



Research on PFN suppression methods in φ -OTDR systems based on the MSI-VPFN algorithm

SHUAI TONG,^{1,2} XINYING ZHAO,³ CHI ZHANG,^{1,2} CHENYANG DING,^{1,2} HAO DING,^{1,2} IMTIAZ NASEEB AWAN,^{1,2} NINGMU ZOU,^{2,4} HUANHUAN LIU,^{2,5} FEI XIONG,^{2,6} YIXIN ZHANG,^{1,2,7} AND XUPING ZHANG^{1,2,8}

¹College of Engineering and Applied Sciences, Nanjing University, Nanjing, 210046, China

²Key Laboratory of Intelligent Optical Sensing and Manipulation, Ministry of Education, Nanjing University, Nanjing, 210093, China

³Nanjing Fiber Technology Co., Ltd., Nanjing, 211135, China

⁴School of Integrated Circuits, Nanjing University, Suzhou, 215163, China

⁵Shenzhen Institute of Advanced Technology, Chinese Academy of Sciences, Shenzhen, 518055, China

⁶Inner Mongolia DT Electric Power Design, Hohhot 010010, China

⁷zyixin@nju.edu.cn

⁸xpzhang@nju.edu.cn

Abstract: The phase-sensitive optical time-domain reflectometry (φ -OTDR) system can monitor the distribution of the acoustic field along the sensing fiber through single-ended access, making it applicable in various fields. However, phase fluctuation noise (PFN) suppression remains a significant challenge. This paper aims to clarify the complex relationship between the signal-to-noise ratio (SNR) of the intermediate frequency (IF) signal and PFN in φ -OTDR systems by quantitatively establishing the nonlinear relationship between the carrier-to-noise ratio (CNR) of the IF signal and the variance of the PFN (VPFN). Accordingly, we propose the MSI-VPFN algorithm, which effectively suppresses PFN by dynamically adjusting spatial weighting according to the standard deviation of VPFN. Compared to the original signal, applying the MSI-VPFN algorithm reduces the PFN standard deviation from 0.386 rad to 0.068 rad and decreases the probability of fading noise from 6.23% to 0.19%. The MSI-VPFN algorithm outperforms traditional methods, providing a scientific basis for evaluating system performance and establishing a solid foundation for the broader application of φ -OTDR technology.

© 2024 Optica Publishing Group under the terms of the [Optica Open Access Publishing Agreement](#)

1. Introduction

The phase-sensitive optical time domain reflectometer (φ -OTDR) has the ability to monitor the distribution of the acoustic field along the sensing fiber through single-ended access. It has advantages such as high sensitivity, wide response band, anti-electromagnetic interference [1]. For these applications that require high-density layout and high-fidelity reconstruction of acoustic field signals, φ -OTDR can provide numerous equivalent sensing units (ESUs) and high multiplexing capability [2]. In recent years, the coherent detection φ -OTDR technology has attracted much attention from researchers. The phase change of weak acoustic signals can be detected because of its high sensitivity, qualitatively and quantitatively reconstruction of the acoustic field signal, and outstanding capabilities in dynamic monitoring [3]. As a result, the technology has been widely applied in various fields, such as pipeline safety protection [4], railway transportation monitoring [5], underwater cable acoustic signal detection [6], and human voice recognition [7].

Despite the numerous benefits of φ -OTDR systems, effectively suppressing noise remains a significant challenge [8]. In φ -OTDR systems, especially those structured around coherent heterodyne detection, the noise mainly comes from the shot noise of the local oscillator (LO) signal, dark current and thermal noise of the photodetector, as well as random quantization noise introduced by the data acquisition card (DAQ) [8,9]. The noise manifests as intensity noise in the intermediate frequency (IF) signal. During the process of phase demodulation, the intensity noise is transformed into phase fluctuation noise (PFN) [10]. The level of PFN is primarily influenced by the signal-to-noise ratio (SNR) of the IF signal [8]. However, due to interference fading, localized low points of the IF SNR can occur in the spatial domain even when the average intensity is high [11]. When the IF SNR is buried in intensity noise, the PFN may encounter great and rapid fluctuations, resulting in significant deviations in phase demodulation results [12,13], and these signals are considered to fall within the fading points.

Digital signal processing (DSP) methods can be used to reduce the impact of PFN. During this process, identifying and suppressing PFN are key challenges. Currently, the identification of fading points mainly relies on empirical thresholds such as the magnitude of IF SNR [8,14–17] or the variation of the PFN (VPFN) [12] for determination. When dealing with fading points, common strategies involve the elimination and filling of such points [8,15]. Directly eliminating identified fading points may transform detectable blind spots into dead zones, causing the system to temporarily lose detection capabilities. A better approach is to use adjacent data in the spatiotemporal domain to fill the fading points. Temporal averaging or filtering can smooth out the rapid fluctuations of PFN in the system, but the temporal resolution and frequency response are also reduced [18]. In spatial weighting processing, the basic idea is to consider the spatial correlation of the signal and the spatial independence of PFN. Typically, adjacent signals in space exhibit higher correlation, while PFN demonstrates lower correlation or independence across different locations. Traditional weighting methods attempt to suppress PFN and enhance the continuity and consistency of signals through weighted averaging. This is primarily achieved through direct phase averaging [19] or spatial weighting based on IF SNR [8]. This approach faces practical challenges in PFN suppression primarily because the weighting process relies on fixed or binary weights. However, demodulation quality depends on IF SNR. It is necessary to adjust the weights dynamically to achieve optimal demodulation quality. Yet, the mathematical relationship between IF SNR and PFN has not been explored in research, partly because directly obtaining IF SNR during the dynamic adjustment process is difficult.

The carrier-to-noise ratio of IF signal (IF CNR) is used to represent IF SNR and the nonlinear monotonic mathematical relationship is revealed between IF CNR and VPFN in this paper. Based on this relationship, the max SNR improvement of the VPFN (MSI-VPFN) algorithm is proposed to provide a method for dynamically adjusting spatial weighting according to the standard deviation of VPFN. Notably, PFN suppression purely through DSP is achieved in this approach, thus avoiding the need for hardware modifications.

2. Principles

2.1. Origins and characteristics of the PFN

In a typical coherent heterodyne detection φ -OTDR system [6], when coherent probe pulses are injected into the fiber, it results in Rayleigh backscattering (RBS) signals. After combining the RBS signal with the LO light signal and bandpass filtering, it is converted into an IF signal. However, due to the spatial distribution and scattering efficiency of different scattering points in the fiber, as well as the influence of random distribution of the optical phase and polarization state changes, the intensity of the RBS signal generated in the coherent superposition process exhibits random fluctuations. During this process, the intensity noise was combined with the IF signal, forming the IF signal carrying intensity noise. The IF signal with noise interference can

be formulated as:

$$I_{IF}(t_k, p_m) = A_s(t_k, p_m) \cos[2\pi f_s \cdot 2p_m/v_g + \varphi_s(t_k, p_m)] + n(t_k, p_m) \quad (1)$$

where t_k is the k th probe pulse, p_m is the length from the starting point of the fiber to the m th ESU, A_s is the amplitude of the IF signal, f_s is the frequency of the IF signal, v_g is the group velocity of the probe pulse in fiber, φ_s is the extra optical phase change acquired as the acoustic field traverses the strained fiber, and n is the intensity noise, it can be expressed as:

$$n(t_k, p_m) = A_n(t_k, p_m) \cos[2\pi f_s \cdot 2p_m/v_g + \phi_n(t_k, p_m)]. \quad (2)$$

where A_n is the noise amplitude, which follows a Rayleigh distribution, and ϕ_n is the noise phase, which follows a uniform distribution, $\phi_n \in [-\pi, \pi]$ [20].

After the amplitude and phase demodulation, the amplitude A and phase φ of the IF signal with noise interference can be obtained by

$$A(t_k, p_m) = \sqrt{A_s^2(t_k, p_m) + A_n^2(t_k, p_m) + 2A_s(t_k, p_m)A_n(t_k, p_m) \cos[\varphi_s(t_k, p_m) - \phi_n(t_k, p_m)]}, \quad (3)$$

$$\begin{aligned} \varphi(t_k, p_m) &= \varphi_s(t_k, p_m) + \varphi_n(t_k, p_m) \\ &= \arctan \left\{ \frac{A_{SNR} \sin[\varphi_s(t_k, p_m)] + \sin[\phi_n(t_k, p_m)]}{A_{SNR} \cos[\varphi_s(t_k, p_m)] + \cos[\phi_n(t_k, p_m)]} \right\}. \end{aligned} \quad (4)$$

where A_{SNR} is the IF SNR, $A_{SNR} = A_s/A_n$, φ_n is the manifestation of intensity noise in the phase domain.

For the φ -OTDR system to capture these local phase changes, spatial differential phase detection is necessary. The differential distance L is considered the spatial resolution of the phase detection and is commonly known as the gauge length [20]. For heterodyne detection systems, the use of highly coherent light sources and phase difference in the spatial domain allows the self-phase noise of the light source to be effectively ignored [21]. Therefore, the local fiber phase change can be expressed as:

$$\Delta\varphi(t_k, p_m) = \Delta\varphi_s(t_k, p_m) + \Delta\varphi_n(t_k, p_m). \quad (5)$$

$\Delta\varphi_n$ is the PFN, $\Delta\varphi_s$ is the phase changes with external disturbances, the linear relationship between the phase change and strain in the fiber can be expressed as:

$$\Delta\varphi_s(t_k, p_m) = 2\alpha\xi \int_{p_m}^{p_m+L} \varepsilon(t_k, x) dx. \quad (6)$$

α is the propagation constant of light in the fiber, $\alpha = 2\pi\eta/\lambda$, η is the effective refractive index of the fiber, λ is the probe pulse wavelength, $\xi = 1 - \eta^2[(1-\mu)p_{12} - \mu p_{11}]/2$, μ is Poisson's ratio, p_{11} , p_{12} are strain-optic tensors, ε is fiber strain [22].

Equation (5) demonstrates that precise measurement of phase changes induced by fiber strain remains unattainable due to the influence of the PFN. Although the intensity noise itself is relatively stable, the IF SNR is not fixed due to the random fluctuations in the intensity of the IF signal. Consequently, the PFN does not remain constant during the actual phase demodulation process. When the IF SNR is high, the PFN level remains stable with relatively small fluctuations. As the IF SNR decreases, the PFN level rises, increasing the Noise Equivalent Power (NEP) of the φ -OTDR system and reducing its ability to detect weak signals. Conversely, when the IF SNR is low, especially when the IF signal is overwhelmed by intensity noise, significant errors may occur in PFN, leading to phase demodulation errors. These fluctuations can result in phase unwrapping failures, distorting the signal and severely degrading the quality of acoustic field restoration.

2.2. Spatial weighting method based on MSI-VPFN

In practical situation, it is hard to accurately and real- timely obtain the true magnitude of the IF SNR due to factors such as fading effects and variations in fiber refractive index. To determine the IF SNR, we can refer to Eq. (3) and construct the following inequality as:

$$\frac{|A_s(t_k, p_m) - A_n(t_k, p_m)|}{A_n(t_k, p_m)} \leq \frac{A(t_k, p_m)}{A_n(t_k, p_m)} \leq \frac{A_s(t_k, p_m) + A_n(t_k, p_m)}{A_n(t_k, p_m)}. \quad (7)$$

and it can be simplified to:

$$|A_{SNR}(t_k, p_m) - 1| \leq A_{CNR}(t_k, p_m) \leq A_{SNR}(t_k, p_m) + 1. \quad (8)$$

where A_{CNR} is the IF CNR, $A_{CNR} = A/A_n$. IF CNR directly reflects the VPFN, indirectly causing changes in PFN. The VPFN from t_k to t_{k+1} can be expressed as:

$$\Delta\varphi'_n(t_k, p_m) = \Delta\varphi'(t_k, p_m) - \Delta\varphi'_s(t_k, p_m). \quad (9)$$

where $\Delta\varphi'$ is the sum of phase variation, $\Delta\varphi'_s$ is the phase variation introduced by acoustic field signals during the same time interval. The IF CNR reflects the standard deviation of VPFN, the relationship is:

$$\sigma_n[\Delta\varphi'_n(t_k, p_m)] = \frac{\sum_{i=1}^N \rho_i A_{CNR}^{N-i}(t_k, p_m)}{\sum_{i=1}^N e_i A_{CNR}^{N-i}(t_k, p_m)}. \quad (10)$$

where σ_n is the standard deviation of VPFN, which is a statistical value, representing the standard deviation of $\Delta\varphi'_n$ under a given A_{CNR} . ρ_i and e_i are the confidences, respectively. Assume there are M-point ESUs in the spatial domain, with the variances of $\Delta\varphi'_s$ at these ESUs are consistent, denoted as σ_s^2 . The SNR of the phase variation at these ESUs can be expressed as:

$$SNR = 10 * \log 10 \left(\frac{\sigma_s^2}{\sigma_n^2} \right). \quad (11)$$

Assume that the variance of $\Delta\varphi'_n$ at these ESUs respectively are $\{\sigma_1^2, \sigma_2^2, \dots, \sigma_{M-1}^2, \sigma_M^2\}$. After M-point spatial weighting processing, the SNR improvement can be calculated as follows:

$$\Delta SNR = 10 * \log 10 \left(\frac{M^2 \sigma_{min}^2}{\sum_{j=1}^M \sigma_j^2} \right). \quad (12)$$

where σ_{min}^2 is the minimum variance among these ESUs. To ensure the suppression of the VPFN, it must satisfy the condition that

$$M\sigma_{min}^2 \leq \sum_{j=1}^M \sigma_j^2 < M^2 \sigma_{min}^2. \quad (13)$$

The calculation of weights primarily depends on the MSI-VPFN. The flowchart is shown in Fig. 1. The MSI-VPFN algorithm process starts with the acquisition of IF signals, followed by demodulation to obtain phase and amplitude information. In the spatial domain, phase information is processed through equidistant differential operations, and phase unwrapping eliminates phase wrapping effects to ensure accurate calculation of local phase variations. Simultaneously, the IF amplitude information is optimized using an equidistant selection method in space. Previous research has shown that the minimum IF amplitude value between two points before and after differential operation strongly reflects signal quality [8]. Thus, this minimum IF amplitude value is chosen to achieve spatial matching of IF amplitude and phase. The IF CNR is defined as the

ratio of the IF amplitude to the intensity noise. And then, the numerical relationship between IF CNR and the variance of VPFN is established through data fitting. Next, IF CNR is obtained to predict the VPFN variance of the M ESUs participating in the spatial weighting operation. Sort the ESUs according to their VPFN variance and evaluate the MSI-VPFN magnitude for spatial weighting from 1 to M points. Finally, use the number of points corresponding to the maximum MSI-VPFN as the number of spatial weighting points at that moment, and perform spatial weighting on the corresponding ESUs to obtain the weighted result. After excluding outliers and applying spatial weighting to the qualifying points, phase integration is performed to obtain the final phase result. Phase unwrapping is then carried out after phase integration to avoid abnormal phase fluctuations caused by excluding outliers, preventing large phase variations between adjacent sampling points.

3. Numerical statistical analysis of IF CNR and VPFN

In Section II of this discussion, we mentioned a clear monotonic relationship between the IF CNR and the VPFN. This section utilizes statistical methods to analyze how this relationship is established.

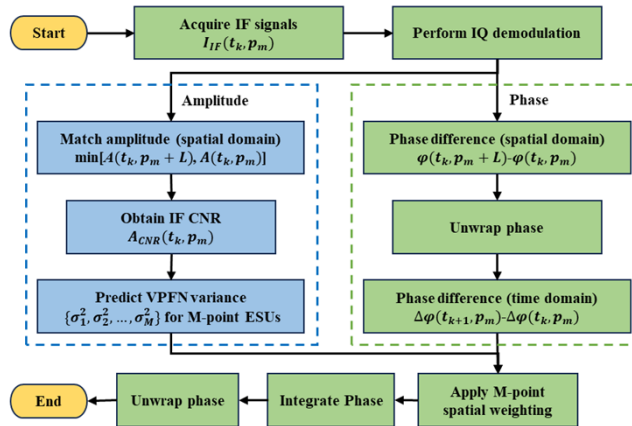


Fig. 1. MSI-VPFN process flowchart.

We set up a standard testing system using a conventional coherent heterodyne detection φ-OTDR system, the schematic diagram as shown in Fig. 2. The narrow linewidth laser (NLL) emits continuous light at 1550.12 nm with a linewidth of 3 kHz and power of 13.1dBm. This light is split by a 90:10 optical coupler (OC1), directing 90% to an acoustic optical modulator (AOM) as probe light, and 10% to a 50:50 2 × 2 optical coupler (OC2) as LO light. Simultaneously, The DAQ generates a 10 MHz sinusoidal reference clock and a 96 ns pulse signal at 1kHz repetition rate, synchronized with the AOM driver. The AOM driver multiplies the clock to 200 MHz, and mixes it with the pulse signal to create an amplitude modulated radio frequency (AM RF) signal that drives the AOM. The AOM shifts the probe light by 200 MHz, producing pulses at 1kHz repetition and 96 ns width, which are amplified by the erbium-doped fiber amplifier (EDFA). These pulses are fed through a circulator (CIR) into the sensing fiber (FUT), where the RBS signal returns through the C port of the CIR and is combined with the LO light through OC2. A balanced photoelectric detector (BPD) with 250 MHz bandwidth converts optical signals to electrical ones, eliminating direct current (DC) bias and common mode noise. The IF signals are then collected by a 250 MS/s DAQ and processed by a computer.

The optical path connection in the experiment is shown in Fig. 3. The system was associated with a 12 km long sensing fiber with a refractive index 1.465. Inside this fiber, FUT1 is 2 km long,

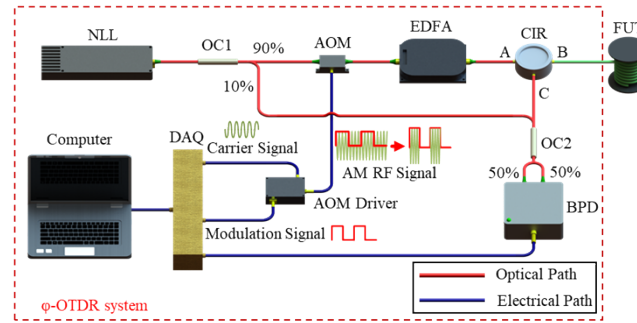


Fig. 2. Schematic diagram of the φ -OTDR system.

and FUT2 extends for 10 km. A piezoelectric transducer (PZT) device, consisting of a 22 m long fiber, was installed between FUT1 and FUT2. To ensure the accuracy of the experimental data, the entire data collection process was performed along the fiber line with minimized vibration, deformation, or temperature changes, and the sine wave driving the PZT was turned off. Upon achieving system stabilization, the collection of signal data returned from the FUT is initiated. Experimental data were captured over the entire fiber during a 10-s interval, consisting of 10,000 IF traces, each trace consisting of 30,000 sampling points, for a total of $10,000 \times 30,000$ data points. All data were processed using statistical methods to ensure stability of results. In the experiment, the demodulation of the φ -OTDR system signal used the IQ demodulation algorithm [15], and an equal distance of 25 sampling points was used, equivalent to a fiber length of 10.2 meters.

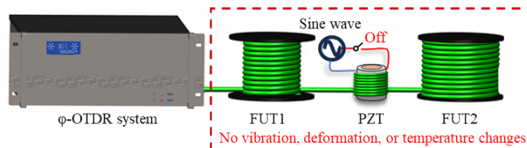


Fig. 3. Experimental setup.

Figure 4 shows the max-normalized probability density (MNPD) distribution of VPFN under varying IF CNR conditions. The MNPD is employed to normalize the probability density, enabling more clear comparisons across different IF CNR levels. At low IF CNR, the VPFN distribution is nearly uniform within the range of $\pm\pi$. As the IF CNR increases, the distribution shifts from uniform to Gaussian. This change is accompanied by a significant narrowing of VPFN fluctuations, indicating greater concentration and stability. This demonstrates that the magnitude of IF CNR directly affects the dispersion of VPFN.

We analyzed the VPFN standard deviation under different IF CNR conditions. Standard deviation is used because it provides a more direct measure of VPFN levels through the amount of dispersion around the mean. Thus, it assists in figuring out the variability and stability of PFN. A larger standard deviation indicates a more dispersed VPFN, indicating a greater effect of PFN, while a smaller standard deviation is associated with a more concentrated VPFN, indicating a lower effect of PFN. Figure 5 shows the experimental data points and their corresponding fitted curves. The VPFN standard deviation decreases as IF CNR increases. At the highest IF CNR level, the minimum standard deviation reaches approximately 0.0715 rad, which is significantly lower than the initial value of 1.8102 rad. By fitting the experimental data to Eq. (10), the data points closely match the fitted curve, from which the corresponding relationship formula was

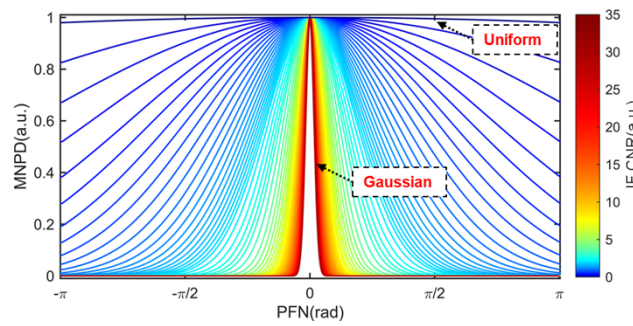


Fig. 4. The MNPD distribution of VPFN under different IF CNR conditions.

derived. The fitted formula for the experimental data is provided in the legend, indicating that the mathematical relationship between VPFN standard deviation and IF CNR is monotonic but nonlinear. The data fitted results are shown in Table 1.

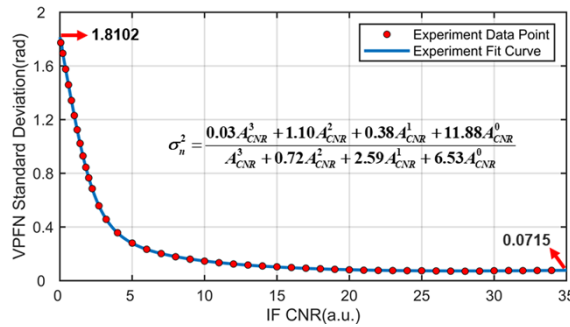


Fig. 5. The standard deviation of VPFN under different IF CNR conditions.

Table 1. Overview of IF CNR and VPFN fit results

Type	Coefficients (with 95% confidence bounds)	Goodness of fit
Experiment	$\rho_1 = 0.034$ (0.026, 0.043)	
	$\rho_2 = 1.099$ (0.809, 1.389)	
	$\rho_3 = 0.384$ (-1.622, 2.391)	SSE:0.000051
	$\rho_4 = 11.881$ (2.841, 20.920)	R-square:0.999996
	$e_1 = 1.000$ (0.992, 1.003)	RMSE:0.001227
	$e_2 = 0.721$ (0.015, 1.426)	AdjustedR-square:0.999994
	$e_3 = 2.591$ (1.901, 3.282)	
	$e_4 = 6.526$ (1.531, 11.521)	

Table 1 provides a detailed overview of the coefficients and goodness-of-fit metrics for experimental data, demonstrating the effectiveness of the fitting models in capturing the behavior of VPFN standard deviation across different IF CNR values. The table shows that the model exhibits outstanding performance, characterized by very low sum of squares due to error (SSE), R-squared values close to 1, and low root mean square error (RMSE). These metrics indicate a strong data-fitting capability, with the adjusted R-squared values also close to 1, confirming the accuracy of the model while maintaining simplicity. This comprehensive analysis confirms that

the fitting model is highly suitable for describing the relationship between IF CNR and VPFN standard deviation. The selection of the fitting order was primarily guided by the SSE, R-squared and RMSE values shown in this table, ensuring an optimal balance between model performance and complexity. It is important to note that higher fitting orders do not necessarily lead to better results and may introduce issues such as overfitting and increased computational complexity. Therefore, a comprehensive evaluation based on practical considerations is necessary.

Continuous operational tests were conducted to assess dynamic fluctuations in the relationship between IF CNR and VPFN and verify model stability. We employed boxplots to visually present the fluctuations in VPFN standard deviation under different IF CNR conditions, ensuring a comprehensive assessment of its statistical stability. Figure 6 reveals the stability of the model over a 48-hour test period. The shaded area in the main plot and the boxplot in the inset demonstrate that fluctuations in VPFN standard deviation remain within a controllable range, indicating that the system maintained good stability throughout the testing period. The zoomed-in view of the boxplot further confirmed the high concentration of data, indicating that the system maintained good stability during long-term operation. These results emphasize the high stability of the model and provide a valuable reference for future system design, ensuring reliability in practical applications.

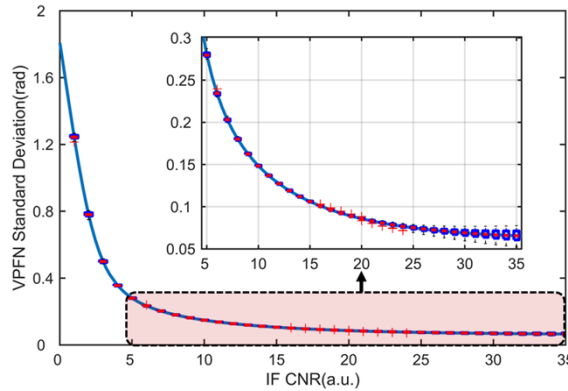


Fig. 6. Model stability analysis.

4. Numerical statistical analysis of noise

4.1. Experimental setup

In order to evaluate the effectiveness of the MSI-VPFN algorithm in suppressing PFN in φ -OTDR systems, the sine wave driving the PZT in Fig. 3 was turned on. The PZT generated vibrational signals with a consistent frequency of 10 Hz and an amplitude of 6 rad. Apart from the disturbance caused by the PZT at the 2 km mark, the data collection was conducted under conditions that minimized vibration, deformation, and temperature changes along the fiber. The total collection time was approximately 350 seconds, yielding 10 billion sampling points. After the data collection, the MSI-VPFN algorithm was applied to analyze the data and assess its ability to suppress PFN under these conditions.

4.2. Results and analysis

Figure 7 presents a 1-second segment of experimental data, highlighting the phase changes over time. In the spatiotemporal map of the original signal, as shown in Fig. 7(a), the PZT-generated vibrational signals are visible at the 2 km mark, yet numerous vertical stripes persist in otherwise

quiet segments, indicating inconsistencies in PFN across different locations. These vertical stripes are typically considered false signals caused by fading noise. Such false signals exhibit a certain degree of randomness in both time and space, posing significant challenges for signal analysis. By applying the MSI-VPFN weighting algorithm, fading noise is effectively suppressed. Figure 7(b) illustrates the effectiveness of the MSI-VPFN algorithm when applied with 25 spatial weighting points in suppressing PFN. In this figure, aside from the vibrational signal at the 2 km mark, the PFN across the entire fiber remains well within ± 1 rad, demonstrating a significant reduction in the impact of fading noise.

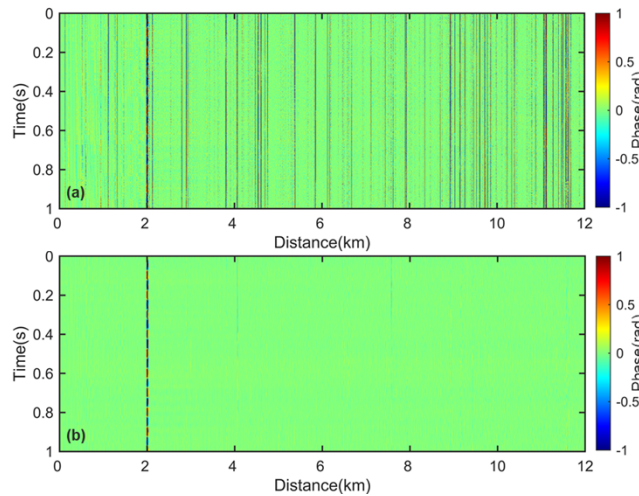


Fig. 7. Spatiotemporal maps of fiber global. (a) Original signal. (b) MSI-VPFN algorithm with 25 spatial weighting points.

Figure 8 shows the localized spatiotemporal maps of vibrational signals under different spatial weighting points. In the original signal shown in Fig. 8(a), in addition to the vibrational signal, false signals are observed at multiple locations due to the lack of weighting. As the number of spatial weighting points increases, the noise in the signal gradually diminishes, and the main signal becomes more distinct and smoother, as shown in Fig. 8(b)–(f).

We analyzed the global phase energy distribution to better compare the impact of different spatial weighting points on fading noise suppression by the MSI-VPFN algorithm. Figure 9(a) shows the phase energy distribution of the original signal. To accurately identify the disturbance locations based on signal power, the original signal exhibits significant fading noise at multiple locations, making it extremely challenging. Figure 9(b) shows the phase energy distribution after applying 25 spatial weighting points. In this case, the noise is initially suppressed as compared to the original signal. However, due to the limited number of weighting points, the suppression effect is not significant, and some noticeable noise peaks remain. As the number of spatial weighting points increases, the noise energy is further reduced, and the main signal peak becomes clear, as illustrated in Fig. 9(c)–(f). Utilizing 25 weighting points nearly achieves perfect noise suppression but results in the lowest spatial resolution. Compared to the original signal, the half-power width remains constant at 12.68 m after spatial weighting, while the signal peak width decreases linearly from 12.28 m to 2.05 m. However, the spatial distribution of the signal expands from 26.18 m to 30.68 m, indicating that the spatial weighting process may cause peak signal energy leakage and degrade spatial distribution. The primary reason is that the signal does not achieve ideal uniformity during spatial weighting, which can be disadvantageous in scenarios requiring high spatial resolution. Therefore, it is essential to strike a balance between noise

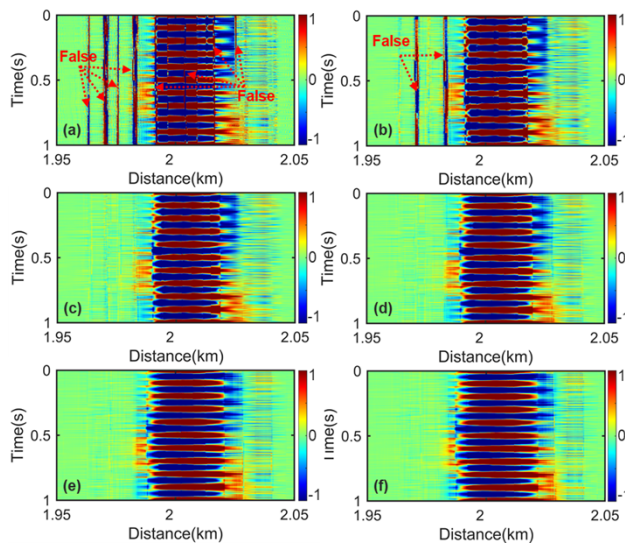


Fig. 8. Spatiotemporal maps of vibrational signals with varying spatial weighting points.
(a) Original signal. (b) 5 points. (c) 10 points. (d) 15 points. (e) 20 points. (f) 25 points.

suppression and spatial resolution when choosing an appropriate number of spatial weighting points for practical applications.

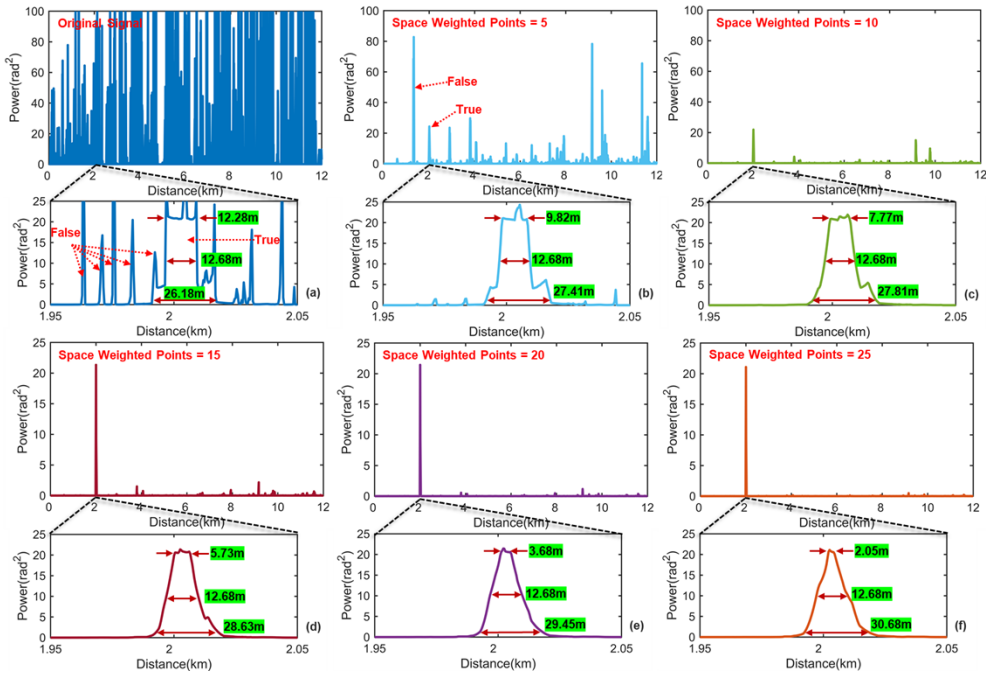


Fig. 9. Phase energy distribution with different numbers of spatial weighting points. (a) Original signal. (b) 5 points. (c) 10 points. (d) 15 points. (e) 20 points. (f) 25 points.

During the experiment, we compared four data processing approaches: the original unweighted signal, referred to as the original signal, phase averaging, IF CNR weighting, and the MSI-VPFN

algorithm. Theoretically, increasing the number of spatial weighting points reduces PFN. Figure 10 illustrates the impact of these methods on PFN suppression with 25 spatial weighting points. Figure 10(a) presents a rescaled version of the original signal from Fig. 7(a) in a 3D view. The vibrational signal is difficult to recognize in the fading noise due to the absence of weighting. The phase averaging method, shown in Fig. 10(b), significantly reduces PFN by averaging multiple sampling points, though it relies on the smoothing effect rather than direct suppression of large PFN, making it less effective when neighboring points have lower PFN. The IF CNR weighting method assigns lower weights to points with higher PFN, further reducing noise, as shown in Fig. 10(c). However, some large PFN values remain. In Fig. 10(d), the MSI-VPFN method effectively eliminates noise that affects PFN optimization, achieving lower and more uniform PFN, in stark contrast to the unweighted method. The results demonstrate that the MSI-VPFN algorithm optimizes the phase demodulation performance by achieving a more uniform and lower PFN distribution than other methods.

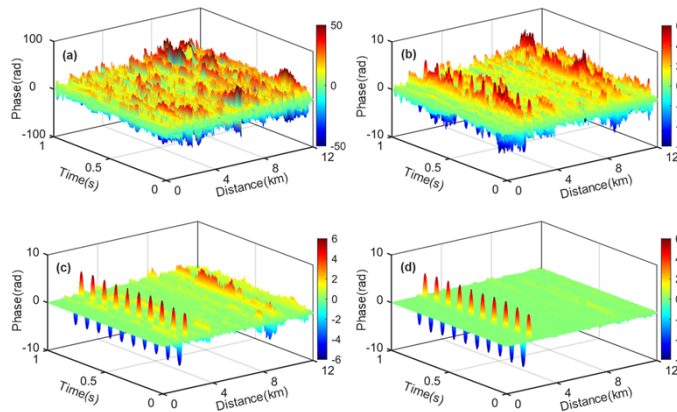


Fig. 10. 3D spatiotemporal phase distribution with 25 spatial weighting points. (a) Original signal. (b) Phase averaging. (c) IF CNR weighting. (d) MSI-VPFN.

We calculated key parameters at locations without vibrational signals over 350 seconds, comparing the performance of different methods in evaluating VPFN and PFN across a range of spatially weighted points from 1 to 25, as shown in Fig. 11. This figure provides a comprehensive comparison of key metrics, highlighting the consistent superiority of the MSI-VPFN algorithm. In Fig. 11(a), the plot illustrates how the VPFN standard deviation varies with the number of spatially weighted points. The original signal with no weighting, exhibits the highest standard deviation of 0.203 rad. The IF CNR weighting and phase averaging methods reduce this to 0.094 rad and 0.110 rad, respectively, but are less effective than the MSI-VPFN algorithm, which achieves a standard deviation of 0.091 rad at 25 points—significantly better than the original signal. This improvement corresponds with an increase in IF CNR from 7 to 17.4, corresponding to the mathematical model in Fig. 4(b). Similarly, Fig. 11(b) illustrates VPFN SNR improvement, with MSI-VPFN leading at a 5.22 dB gain, followed by IF CNR weighting at 5.03 dB and phase averaging at 3.89 dB. The original signal shows no improvement without spatial weighting. Overall, the analysis indicates that the MSI-VPFN algorithm outperforms the other methods in reducing VPFN standard deviation and enhancing SNR, particularly as the number of spatially weighted points increases, demonstrating its efficacy in optimizing signal quality through effective VPFN suppression.

The VPFN represents the fluctuations of PFN, but in practice, more attention is given to the magnitude of PFN. Similar to the previous analysis of VPFN, the MSI-VPFN algorithm once again demonstrates superior performance, achieving the lowest PFN standard deviation of 0.068

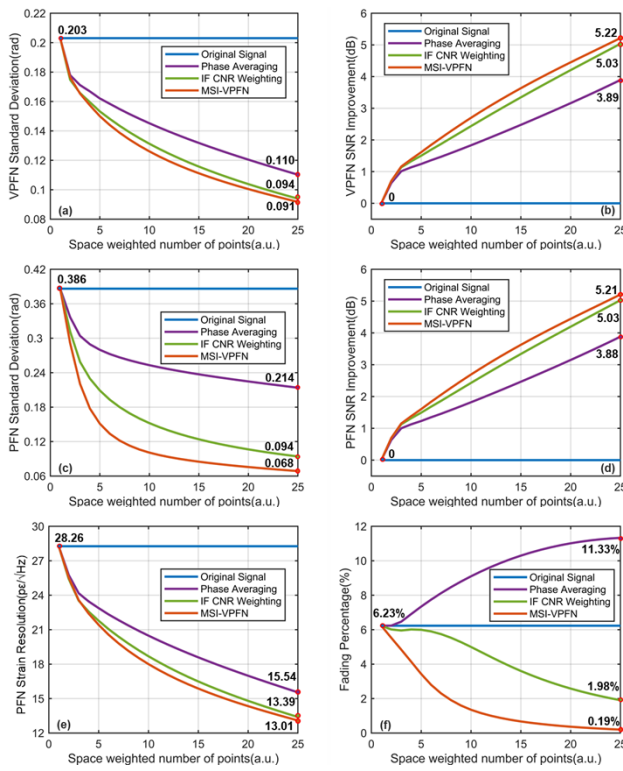


Fig. 11. Comparison of key parameters among different algorithms for spatial weighting points. (a) VPFN standard deviation. (b) VPFN SNR improvement. (c) PFN standard deviation. (d) PFN SNR improvement. (e) PFN strain resolution. (f) Fading percentage.

rad at 25 points, as shown in Fig. 11(c). This marks a significant improvement compared to the original signal, which has the highest standard deviation of 0.386 rad. The phase averaging and IF CNR weighting methods also show considerable reductions in PFN standard deviation but are less effective than MSI-VPFN, their effectiveness and suppression rate are far inferior to the MSI-VPFN algorithm, with final values of 0.094 rad and 0.214 rad, respectively. The MSI-VPFN algorithm effectively suppresses PFN, leading to significant improvements in system performance, stability, and reliability. Figure 11(d) illustrates the MSI-VPFN algorithm achieves the highest SNR improvement of 5.21 dB at 25 points, outperforming both the IF CNR weighting and phase averaging methods, which reach 5.03 dB and 3.88 dB, respectively. It is worth noting that the improvements in both VPFN SNR and PFN SNR are highly consistent, indirectly confirming the rationale of using VPFN as a spatial weighting factor.

The reduction in PFN significantly benefits the system in two key ways. First, it lowers the NEP of the φ -OTDR system as shown in Fig. 11(e), markedly enhancing its detection sensitivity. In our statistical analysis of a 12 km fiber span with 25 spatial weighting points, the MSI-VPFN, IF CNR weighting, and phase averaging methods improved the strain resolution from $28.2\text{pe}/\sqrt{\text{Hz}}$ to $15.54\text{ pe}/\sqrt{\text{Hz}}$, $13.39\text{ pe}/\sqrt{\text{Hz}}$, and $13.01\text{ pe}/\sqrt{\text{Hz}}$, respectively, indicating a substantial optimization of the system's detection performance. It was also observed that increasing the number of spatial weighting points further enhances strain resolution. Second, reducing PFN helps decelerate fading noise, resulting in greater phase stability and fewer false disturbance signals, thereby improving the overall performance and accuracy of φ -OTDR systems for various applications. In this study, we assume that fading noise is present when the phase noise exceeds

a PFN standard deviation of 0.386 rad, which we define as the threshold for fading noise. Using this criterion, we analyzed the suppression of fading noise under different numbers of spatially weighted points, as shown in Fig. 11(f). The MSI-VPFN algorithm demonstrates the most significant suppression of fading noise, reducing the fading percentage to just 0.19%, a dramatic improvement from the original signal's 6.23%. The MSI-VPFN algorithm not only achieves the lowest fading percentage but also exhibits the fastest suppression rate. In comparison, the IF CNR weighting method lowers the fading percentage to 1.98%, while the phase averaging method, counterintuitively, increases it to 11.33%. These results highlight the superior effectiveness of the MSI-VPFN algorithm in minimizing fading noise and maintaining signal integrity.

Finally, keeping all other experimental parameters unchanged, we adjusted the PZT to generate vibration signals at different frequencies and compared the SNR improvement achieved by three spatial weighting methods. In this analysis, spatial weighting was performed over 25 points around the vibration location. The SNR is defined as the ratio of the energy of the applied vibration signal to the noise energy, and the SNR improvement represents the difference between the SNR of the original signal and that after applying each algorithm. As shown in Fig. 12, the MSI-VPFN algorithm consistently outperforms the other two methods over all the vibration frequencies tested and demonstrates the most significant SNR improvement, highlighting its ability to dynamically adapt and effectively suppress phase fluctuation noise under varying vibration conditions. These results further confirmed the advantages of the MSI-VPFN algorithm in improving signal quality in a wide range of operational conditions.

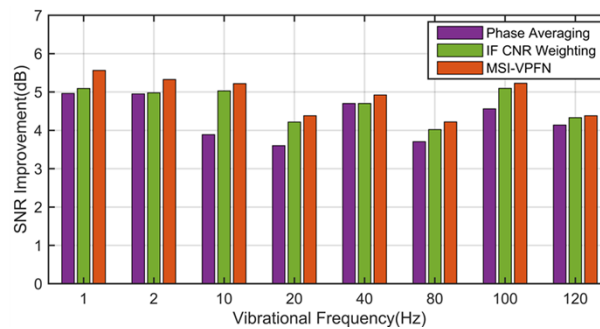


Fig. 12. Comparison of SNR improvement across different vibration frequencies with different algorithms.

5. Conclusion

This study has successfully addressed the PFN challenge in φ -OTDR systems through theoretical modeling and experimental validation while enhancing signal integrity without the need for hardware upgrades. The innovations, including the modeling of the IF CNR-VPFN relationship and the MSI-VPFN algorithm for PFN suppression, will provide a practical solution and pave the way for advancements in distributed fiber sensing technology, particularly in complex environments.

Funding. National Natural Science Foundation of China (U2001601, 62175100); Equipping Pre-research Project (30601010104); Fundamental Research Funds for the Central Universities (2024300447, 0213-14380211); General Program of Shenzhen Science, Technology & Innovation Commission (JCYJ20220530113811026); Shenzhen Research Foundation under Grant (KJZD20230923114601003); CAS Pioneer Hundred Talents Program; Shenzhen Science and Technology Program (JSGGKQTD20221101115656030).

Disclosures. The authors declare no conflicts of interest.

Data availability. Data underlying the results presented in this paper are not publicly available at this time but may be obtained from the authors upon reasonable request.

References

1. X. Bao and L Chen, "Recent Progress in Distributed Fiber Optic Sensors," *Sensors* **12**(7), 8601–8639 (2012).
2. Z. Ding, N. Zou, C. Zhang, *et al.*, "Self-Optimized Vibration Localization Based on Distributed Acoustic Sensing and Existing Underground Optical Cables," *J. Lightwave Technol.* **40**(3), 844–854 (2022).
3. G. Haniel and E. Avishay, "On the Sensitivity of Distributed Acoustic Sensing," *Opt. Lett.* **41**(24), 5648–5651 (2016).
4. T. Javier, M.G. Javier, M. Hugo, *et al.*, "A Novel Fiber Optic Based Surveillance System for Prevention of Pipeline Integrity Threats," *Sensors* **17**(2), 355 (2017).
5. C. Du, S. Dutta, P. Kurup, *et al.*, "A Review of Railway Infrastructure Monitoring using Fiber Optic Sensors," *Sens. Actuators* **303**, 111728 (2020).
6. X. Chen, N. Zou, Y. Wan, *et al.*, "On-Line Status Monitoring and Surrounding Environment Perception of An Underwater Cable Based on the Phase-Locked Φ -OTDR Sensing System," *Opt. Express* **30**(17), 30312–30330 (2022).
7. Y. Wu, J. Gan, Q. Li, *et al.*, "Distributed Fiber Voice Sensor Based on Phase-Sensitive Optical Time-Domain Reflectometry," *IEEE Photonics J.* **7**(6), 1–10 (2015).
8. X. Zhang, Q. Wang, F. Xiong, *et al.*, "Performance Enhancement Method for Phase-Sensitive Optical Time-Domain Reflectometer System Based on Suppression of Fading Induced False Alarms," *Opt. Eng.* **59**(04), 46101 (2020).
9. LD van Putten, A Masoudi, G. Snook, *et al.*, "Numerical Modelling of a Distributed Acoustic Sensor Based on Ultra-Low Loss-Enhanced Backscattering Fibers," *Sensors* **21**(20), 6869 (2021).
10. S. Lin, Z. Wang, J. Xiong, *et al.*, "Rayleigh Fading Suppression in One-Dimensional Optical Scatters," *IEEE Access* **7**, 17125–17132 (2019).
11. A. Eyal and H. Gabai, "Distributed Acoustic Sensing: How to Make The Best Out of The Rayleigh-Backscattered Energy?" *2017 25th Optical Fiber Sensors Conference*, 1–4 (2017).
12. F. Pang, M. He, H. Liu, *et al.*, "A Fading-Discrimination Method for Distributed Vibration Sensor Using Coherent Detection of φ -OTDR," *IEEE Photonics Technol. Lett.* **28**(23), 2752–2755 (2016).
13. H. He, L. Yan, H. Qian, *et al.*, "Suppression of the Interference Fading in Phase-Sensitive OTDR With Phase-Shift Transform," *J. Lightwave Technol.* **39**(1), 295–302 (2021).
14. Y. Zhang, J. Liu, F. Xiong, *et al.*, "A Space-Division Multiplexing Method for Fading Noise Suppression in the Φ -OTDR System," *Sensors* **21**(5), 1694 (2021).
15. M. Zabihi, Y. Chen, T. Zhou, *et al.*, "Continuous Fading Suppression Method for Φ -OTDR Systems Using Optimum Tracking over Multiple Probe Frequencies," *J. Lightwave Technol.* **37**(14), 3602–3610 (2019).
16. J. Zhou, Z. Pan, Q. Ye, *et al.*, "Characteristics and Explanations of Interference Fading of a Φ -OTDR With a Multi-Frequency Source," *J. Lightwave Technol.* **31**(17), 2947–2954 (2013).
17. A.H. Hartog, L.B. Liokumovich, N.A. Ushakov, *et al.*, "The Use of Multi-Frequency Acquisition to Significantly Improve the Quality of Fibre-Optic-Distributed Vibration Sensing," *Geophys. Prospect.* **66**(S1), 192–202 (2018).
18. X. Zhang, Y. Zheng, C. Zhang, *et al.*, "A Fading Tolerant Phase-Sensitive Optical Time Domain Reflectometry Based on Phasing-Locking Structure," *Electronics* **10**(5), 535 (2021).
19. Z. Ding, S. Wang, J. Kang, *et al.*, "Distributed Acoustic Sensing-Based Weight Measurement Method," *J. Lightwave Technol.* **42**(9), 3454–3460 (2024).
20. A.E. Alekseev, B.G. Gorshkov, V.T. Potapov, *et al.*, "Random Jumps in The Phase-OTDR Response," *Appl. Opt.* **61**(1), 231–240 (2022).
21. Z. Xiao, J. Chen, J. Ji, *et al.*, "Complete Phase Noise Compensation for 50 km DAS with 100 kHz linewidth ITLA," in *28th Int. Conf. Opt. Fiber Sensors, Technical Digest Series* (Optica Publishing Group) F2.1 (2023).
22. A. H. Hartog, "An introduction to distributed optical fibre sensors," *CRC press* **266**, 472 (2017).